



# Numerical investigation on heat transfer of a nano-fluid saturated vertical composite porous channel packed between two fluid layers

Pulla Nagabhushana<sup>1</sup> · S. Ramprasad<sup>2</sup> · C. Durga Prasad<sup>1</sup> · Hitesh Vasudev<sup>3</sup> · Chander Prakash<sup>3</sup>

Received: 4 February 2023 / Accepted: 17 May 2023 / Published online: 6 June 2023  
© The Author(s), under exclusive licence to Springer-Verlag France SAS, part of Springer Nature 2023

## Abstract

This numerical study investigates the effect of internal heat on heat transfer in a nanofluid saturated vertical channel with a porous matrix layer sandwiched between two fluid layers. The Darcy–Forchheimer equation is used to model flow in a porous material. To characterize the nanofluid, the Tiwari and Das model is used. The transport parameters of the fluids are constant in all three locations. The Finite element Galerkin method is used to convert governing equations into systems of equations. The behavior of nanofluid is investigated by taking the solid volume fraction into account. The flow characteristics were investigated for various values of the relevant parameters in the model, which includes Grashof number, Brinkman number, solid volume fraction, porous parameter, interphase heat transfer, internal heat generation, Forchheimer parameter, nanofluid to solid porous matrix thermal conductivity ratio parameter, porosity of the medium using water as the base fluid and copper as the nanoparticle. To study flow and heat transmission, five different types of nanoparticles are used. Silver nanoparticles achieve the maximum value of the Nusselt number.

**Keywords** Nanofluid · Internal heat · Porous-matrix · Darcy–Forchheimer model · LTNE · ANN model

## 1 Introduction

Three phase flows are important in several industrial contexts. Flow forms in three phase flows are intricate and differ considerably from system to system. A multiphase flow system is one in which distinct phases exist at the same time, with a two-phase system being the simplest form. Even though the oil industry is the primary driver of research in this area, multiphase flow in porous media continues to attract a lot of attention because it occurs in a wide range of engineering disciplines. It is also dominant in many natural phenomena, for example, sediment transport in rivers is subject to multiphase flow. When compared to single-phase flow, characterizing, and quantifying the nature of the flow is significantly more

difficult due to the presence of many phases. Due to a lack of understanding about the velocities of each phase at a single site and varied mechanisms regulating them, the velocity distribution is difficult to compute. As a result, it's critical to comprehend the nature and behavior of flow in multiphase systems.

Multiphase flows are not limited to three phases, direct-contact freeze crystallization is an example of a four-phase flow system. Practically all processing technologies, from cavitating pumps and turbines to electro photographic processes, papermaking, and the pellet form of almost all raw polymers, must cope with the multiphase flow. The majority of problems in the geophysics, petroleum industry, plasma physics, and other related fields involve multi fluid flow scenarios. Three-phase flows appear in a wide range of industrial processes, from the production stages of oil and gas Bello et al. [1], in the transport of biomass Miao et al. [2] or some chemical reactors Scott and Rao [3], nuclear waste decommissioning Mao et al. [4], pulp and paper production, and in various applications of air injections Orell [5]. Thus, it's critical to optimize three-phase flows, which is a process with plenty of space for improvement Ghasemi [6].

✉ C. Durga Prasad  
durgapras71@gmail.com

✉ Hitesh Vasudev  
hitesh.24804@lpu.co.in

<sup>1</sup> RV Institute of Technology and Management, Bengaluru, Karnataka, India

<sup>2</sup> M S Ramaiah Institute of Technology, Bengaluru, Karnataka, India

<sup>3</sup> Lovely Professional University, Phagwara, India

Vafai and Kim [7] offered the first accurate solution for fluid flow in the interface region. The fluid flow and heat-transfer interfacial conditions between a porous medium and a fluid layer were studied by Alzami and Vafai [8]. Porosity formation in solidifying castings of the mushy zone for three phase model was studied by Kuznetsov and Vafai [9]. Comparison of various formulations of three phase flow in porous media was established by Zhangxim and Richord [10]. Authors have discussed various formulations of the governing equations which describe three phase flow in porous media which includes phase, global and pseudo-global pressure saturation formulations, and have presented theoretically and numerically.

Malashetty et al. [11, 12] analyzed one and two fluid flow models for permeable fluid in horizontal and inclined channels. Frontiers and progress in multiphase flow and heat transfer was presented by Cheng and Ghajar. [13]. Multiphase modeling techniques and their challenges can be understood from multiphase-flows in biomedical applications by Jingliang Dong et al. [14]. Umavathi et al. [15–17] analyzed fluid flow models sandwiched between viscous fluids in horizontal and vertical channels. Umavathi and Hemvathi [18] examined convective flow in a vertical porous channel saturated with nanofluid packed between viscous fluid layers recently. The results showed that silver as a nanoparticle had the optimum velocity while titanium oxide had the least velocity. Recently Patra and Nayak [19], Satish and Kishan [20] are study the effects of nonfluids. Hoseinzadeh [21] examined the effect of varied channel cross-sectional geometries on pulsating flow in a three-dimensional channel employing alumina nanofluid with varying volume percentages as a working fluid. It is observed that when the volume proportion of nanoparticles increases, the fluid temperature decreases.

Only sluggish flows in porous media with low permeability are suitable for the Darcy model, Nakayama et al. [22]. Many advanced applications of porous media have high flow velocities. Inertial effects become important at greater flow rates or in hyper porous media Bear [23]. The momentum equation for porous medium must account for divergence from linearity in such cases. This divergence is caused by Forchheimer's term, which reflects quadratic drag. From a physical aspect, quadratic drag emerges in the momentum equation for porous media because the form of drag owing to solid barriers becomes comparable to surface drag due to friction at high filtration velocities Nield and Bejan [24].

Internal heat generation inside both the solid and fluid phases has recently been highlighted as having an impact on the temperature field inside the porous medium [25–31]. Internal heat generation and absorption can occur from a variety of causes, including viscous heating in both the solid and fluid phases of a porous material. Heat generation/absorptions occur as source/sink terms in the energy

conversation equations of a porous material's solid and fluid phases, making these equations non-homogeneous. As a result, getting an analytical solution to such issues becomes more challenging. Yang and Vafai [27] examined the influence of constant internal heat generation on the temperature field in the porous medium under LTNE in the fully developed region of a porous channel. It is established that the internal heat generation in the solid phase is important for characteristics of heat transfer.

Because of many practical applications, porous-media with high flow velocities and the possibility of occurrence of internal heat generation due to viscous heating is involved, the work of Umavathi and Hemavathi [18] was extended to study the effect of internal heat generation on the flow and heat transfer of a nanofluid (water as base fluid and copper as nanoparticle) saturated composite porous medium sandwiched between two fluid layers, which has not been previously addressed. In this paper we have investigated a numerical analysis of heat transfer characteristics of nano fluids on different models which are related to industrial system applications such as heat exchangers, heat storage, geothermal systems, and drying techniques. This paper is related to designing of industrial systems and studying of its heat transfer characteristics. Further, in this study, local thermal non-equilibrium (LTNE) conditions were adopted in the middle region of the system, because when high flow velocities are involved, fluid and solid phases of the porous material are at different temperatures. The flow and heat transfer characteristics depend on Grashof number  $Gr$ , Brinkman number  $Br$ , solid volume fraction  $\phi$ , porous parameter  $\sigma$ , interphase heat transfer  $H$ , internal heat generation  $w_s$ , Forchheimer parameter  $F$ , nanofluid to solid porous-matrix thermal conductivity ratio parameter  $k_r$ , porosity  $\varepsilon$  of the medium. The momentum and energy equations are coupled and nonlinear in respective regions. Galerkin finite element method is used to solve these equations to obtain Nusselt number profiles. For the current study, an ANN model is suggested to forecast heat transfer for various parameters included in the investigation Hoseinzadeh et al. [32].

## 2 Mathematical formulation

Figure 1 depicts the physical configuration. The flow of three immiscible fluids in a vertical channel has been studied as a continuous, laminar mixed convective flow. The X-axis is taken parallel to the channel, while the Y-axis is taken perpendicular to it. The region  $0 \leq y \leq L$  is occupied by the Nanofluid and the regions  $-L \leq y \leq 0$ ,  $L \leq y \leq 2L$  are occupied by the viscous fluid. The flow in all three regions is assumed to be incompressible and fully developed. The thermo physical properties are assumed to be constant except

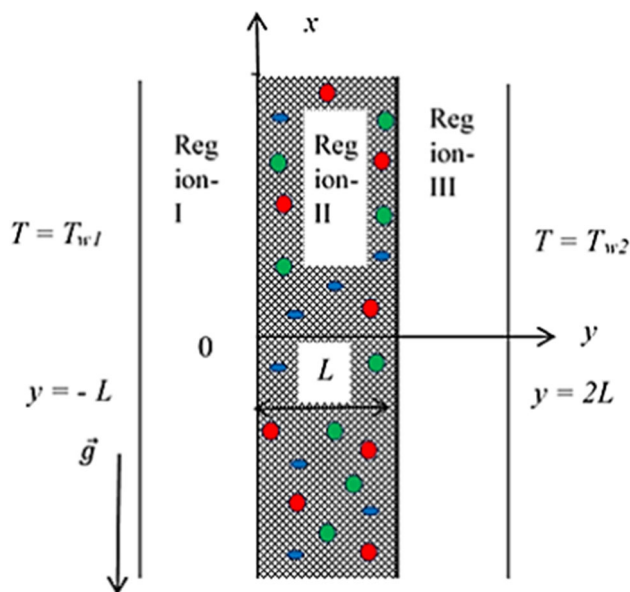


Fig. 1 Physical model

for the density in the buoyancy term in the momentum equation. The fluid rises in the channel driven by buoyancy forces.

Both regular and nanofluid transport characteristics are considered to be constant. The channel’s boundary walls are kept at distinct constant temperatures, i.e.,  $T_{w1}$  at the left wall and  $T_{w2}$  at the right wall with  $T_{w1} \geq T_{w2}$ . We have assumed the Boussinesq approximation. Further, it is presumed that at the two interphases there is continuity of velocity, temperature, and heat fluxes. With these assumptions and also employing the nanofluid model recommended by Tiwari and Das [33], the momentum and energy equations are adopted from Ghasemi and Aminossadati [34], Muthamilselvan et al. [35], Vajravelu et al. [36], Yasser Mahmoudi [25].

To solve problems involving nanofluids mathematically, two types of models are used. One is a single-phase model, while the other is a two-phase one. The Tiwari and Das model is an example of a single-phase model. In a single phase model, the fluid, velocity, and temperature are all considered to be the same. In the two-phase model, the fluid velocity and the temperature of the nanoparticles are assumed to be different. The single-phase model has the advantage of being simpler and easier to solve numerically because the slip processes are ignored. In the Tiwari and Das model volume concentration of nanoparticles ranges between 3 and 20%.

### 2.1 Physical domain

### 2.2 Governing equations

Region-I

$$\frac{dv_1}{dy} = 0 \tag{1}$$

$$\mu_f \frac{d^2u_1}{dy^2} + \rho_f g \beta_f (T_1 - T_{w2}) - \frac{\partial p}{\partial x} = 0 \tag{2}$$

$$K_f \frac{d^2T_1}{dy^2} + \mu_f \left( \frac{du_1}{dy} \right)^2 = 0 \tag{3}$$

Region-II

$$\frac{dv_2}{dy} = 0 \tag{4}$$

$$\begin{aligned} -\frac{\partial p}{\partial x} + \mu_{nf} \frac{d^2u_2}{dy^2} + \rho_{nf} g \beta_{nf} (T_2 - T_{w2}) \\ - \frac{\mu_{nf}}{k} u_2 - \frac{\rho_{nf} C_1}{\sqrt{k}} u_2^2 = 0 \end{aligned} \tag{5}$$

$$\begin{aligned} K_{nf} \frac{d^2T_{2f}}{dy^2} + \mu_{nf} \left( \frac{du_2}{dy} \right)^2 + \frac{\mu_{nf}}{k} u_2^2 \\ + \frac{h_{nfs}}{\varepsilon(\rho c)_{nf}} (T_s - T_{nf}) + s_f = 0 \end{aligned} \tag{6}$$

$$K_s \frac{d^2T_{2s}}{dy^2} + \frac{h_{nfs}}{(1 - \varepsilon)(\rho c)_s} (T_{nf} - T_s) + s_s = 0 \tag{7}$$

Region-III

$$\frac{dv_3}{dy} = 0 \tag{8}$$

$$\mu_f \frac{d^2u_3}{dy^2} + \rho_f g \beta_f (T_3 - T_{w2}) - \frac{\partial p}{\partial x} = 0 \tag{9}$$

$$K_f \frac{d^2T_3}{dy^2} + \mu_f \left( \frac{du_3}{dy} \right)^2 = 0 \tag{10}$$

Following are the boundary and interface conditions for the velocity and temperature as in [37]

### 2.3 Boundary conditions

$$\begin{aligned} u_1(-L) = 0, u_1(0) = u_2(0), \\ \mu_f \frac{du_1(0)}{dy} = \mu_{nf} \frac{du_2(0)}{dy}, u_2(L) \\ = u_3(L), \mu_{nf} \frac{du_2(L)}{dy} = \mu_f \frac{du_3(L)}{dy}, u_3(2L) = 0 \end{aligned} \tag{11}$$

$$\begin{aligned} T_1(-L) = T_{w2}, T_1(0) = T_2(0), \\ K_f \frac{dT_1(0)}{dy} = K_{nf} \frac{dT_2(0)}{dy}, T_2(L) = T_3(L), \\ K_{nf} \frac{dT_2(L)}{dy} = K_f \frac{dT_3(L)}{dy}, T_3(2L) = T_{w1} \end{aligned} \tag{12}$$

The effective density of nanofluid is given by

$$\rho_{nf} = (1 - \phi)\rho_f + \phi\rho_s \quad (13)$$

The thermal diffusivity, heat capacitance and thermal expansion coefficients of the nanofluid are given by

$$\alpha_{nf} = \frac{k_{nf}}{(\rho C_p)_{nf}} \quad (14)$$

$$(\rho C_p)_{nf} = (1 - \phi)(\rho C_p)_f + \phi(\rho C_p)_s \quad (15)$$

$$(\rho\beta)_{nf} = (1 - \phi)(\rho\beta)_f + \phi(\rho\beta)_s \quad (16)$$

The effective dynamic viscosity of the nanofluid is given by [38]

$$\mu_{nf} = \frac{\mu_f}{(1 - \phi)^{2.5}} \quad (17)$$

For spherical nanoparticles, according to Maxwell [39], this can be written as

$$K_{nf} = K_f \frac{K_s + 2K_f - 2\phi(K_f - K_s)}{K_s + 2K_f + \phi(K_f - K_s)} \quad (18)$$

To transform the Eqs. (1)–(12) in to dimensionless form, we introduce the following dimensionless parameters

$$y^* = \frac{y}{L}, u_i^* = u_i \left( \frac{\rho_f}{\mu_f} \right) L, \quad (19a)$$

$$\theta_i = \frac{T_i - T_{w2}}{T_{w1} - T_{w2}}, \theta_{nf2} = \frac{T_{nf2} - T_{w2}}{T_{w1} - T_{w2}}, \theta_{s2} = \frac{T_{s2} - T_{w2}}{T_{w1} - T_{w2}}, \quad (19b)$$

$$Gr = \frac{g\beta_f(T_{w1} - T_{w2})L^3}{v_f^2}, Br = \frac{\mu_f^3}{\rho_f^2 L^2 (T_{w1} - T_{w2}) k_f}, P = -\frac{\rho_f L^3}{\mu_f^2} \frac{\partial P}{\partial x}, \quad (19c)$$

$$\sigma = \frac{L}{\sqrt{k}}, F = \frac{\rho_{nf} C_I u_i L^2}{\mu_{nf} \sqrt{K}}, H = \frac{h_{nfs} L^2}{K_{nf}}, k_r = \frac{K_{nf}}{(1 - \varepsilon) K_s}, \quad (19d)$$

$$w_f = bs_f, w_s = Hk_r s_s \quad (19e)$$

Substituting the above quantities in to Eqs. (1)–(12), after dropping asterisks we get the following non-dimensionalized equations.

Region-I

$$\frac{d^2 u_1}{dy^2} + Gr\theta_1 + P = 0 \quad (20)$$

$$\frac{d^2 \theta_1}{dy^2} + Br \left( \frac{du_1}{dy} \right)^2 = 0 \quad (21)$$

Region-II

$$\frac{d^2 u_2}{dy^2} + Gr\theta_{2nf} - \sigma^2 u_2 + P(1 - \phi)^{2.5} - Fu_2^2 = 0 \quad (22)$$

$$\frac{d^2 \theta_{2nf}}{dy^2} + Brb \left[ \left( \frac{du_2}{dy} \right)^2 + \sigma^2 u_2^2 \right] + \frac{H}{\varepsilon} (\theta_{2s} - \theta_{2nf}) + w_f = 0 \quad (23)$$

$$\frac{d^2 \theta_{2s}}{dy^2} + Hk_r (\theta_{2nf} - \theta_{2s}) + w_s = 0 \quad (24)$$

Region-III

$$\frac{d^2 u_3}{dy^2} + Gr\theta_3 + P = 0 \quad (25)$$

$$\frac{d^2 \theta_3}{dy^2} + Br \left( \frac{du_3}{dy} \right)^2 = 0 \quad (26)$$

where

$$a = (1 - \phi)^{2.5} \left[ (1 - \phi) + \frac{\phi(\rho\beta)_s}{(\rho\beta)_f} \right], bb = \frac{1}{(1 - \phi)^{2.5}} \left( \frac{K_s + 2K_f + \phi(K_f - K_s)}{K_s + 2K_f - 2\phi(K_f - K_s)} \right), \quad (27)$$

In the non-dimensional form, the boundary and interface conditions become

$$u_1(-1) = 0, u_1(0) = u_2(0), \frac{du_1(0)}{dy} = \frac{\mu_{nf}}{\mu_f} \frac{du_2(0)}{dy}, u_2(1) = u_3(1), \frac{du_2(1)}{dy} = \frac{\mu_f}{\mu_{nf}} \frac{du_3(1)}{dy}, u_3(2) = 0 \quad (28)$$

$$\theta_1(-1) = \theta_{w2}, \theta_1(0) = \theta_2(0), \frac{d\theta_1(0)}{dy} = \frac{K_{nf}}{K_f} \frac{d\theta_2(0)}{dy}, \theta_2(1) = \theta_3(1), \frac{d\theta_2(1)}{dy} = \frac{K_f}{K_{nf}} \frac{d\theta_3(1)}{dy}, \theta_3(2) = \theta_{w1}, \theta_{wr} = \frac{\theta_{w1}}{\theta_{w2}}. \quad (29)$$

The Nusselt number, which is given in [37, 40], can be used to predict the heat transfer rate at the microporous channel.

$$\begin{aligned} Nu_{u1} &= \frac{q_{w1}(2L)}{k_1(T_{w1} - T_{1,m})} = \frac{2}{\theta_{1,m}}, \quad Nu_{2nf} \\ &= \frac{q_{w2}(2L)}{k_{2f}(T_{w2} - T_{2f,m})} = \frac{2}{\theta_{2nf,m}}, \\ Nu_{u3} &= \frac{q_{w2}(2L)}{k_3(T_{w2} - T_{3,m})} = \frac{2}{\theta_{3,m}} \end{aligned} \quad (30)$$

where  $\theta_{1,m} = \frac{\int_{-1}^0 u_1 \theta_1 dy}{\int_{-1}^0 u_1 dy}$ ,  $\theta_{2nf,m} = \frac{\int_0^1 u_2 \theta_{2nf} dy}{\int_0^1 u_2 dy}$ ,  $\theta_{3,m} = \frac{\int_1^2 u_3 \theta_3 dy}{\int_1^2 u_3 dy}$  is the dimensionless mean temperature difference.

$$Nu_{avg} = \frac{q_{wi}(3L)}{k_{fi}(T_{wi} - T_{if,m})} = \frac{3}{\theta_{avg,m}} \quad (31)$$

where  $\theta_{avg,m} = \frac{\int_{-1}^0 u_1 \theta_1 dy + \int_0^1 u_2 \theta_{2nf} dy + \int_1^2 u_3 \theta_3 dy}{\int_{-1}^0 u_1 dy + \int_0^1 u_2 dy + \int_1^2 u_3 dy}$  is the dimensionless mean temperature.

### 3 Numerical scheme

To predict the heat transfer behavior in the porous medium, Eqs. (20)–(26) are solved using the Finite element method (FEM). The Galerkin method is used to obtain matrix form equations from governing equations. A simple linear element with two nodes is used within the element to represent variations in the velocity and temperature functions. The values of  $u$ ,  $\theta_f$  and  $\theta_s$  that vary within the element are written as [37, 41].

$$u = u_i N_i + u_j N_j, \quad \theta_f = \theta_{fi} N_i + \theta_{fj} N_j, \quad \theta_s = \theta_{si} N_i + \theta_{sj} N_j \quad (32)$$

where  $N_i = \frac{y_j - y}{y_j - y_i}$ ,  $N_j = \frac{y - y_i}{y_j - y_i}$ .

Using the FEM formulation, Eqs. (20)–(26) are converted into matrix form equations for the elements, as in [41]. The coupled matrix equations for the elements are combined to obtain the global matrix for the entire domain, which is solved iteratively to obtain  $u$ ,  $\theta_f$  and  $\theta_s$  in the porous medium. To obtain converged results, the error level of solution for  $u$ ,  $\theta_f$  and  $\theta_s$  are set to  $10^{-4}$ . When the above-mentioned error level, which is the difference between previous and current iterations for a variable at all nodes, is reached, the iterative process is terminated.

#### 3.1 Validation

As observed in Table 1 the obtained  $Nu$  values in the present study at the channel walls  $y = -1$  and  $y = 2$  for different

values of  $Gr$  are compared with Umavathi and Hemvathi [18] and also Ansys simulations and found in good agreement.

## 4 Results and discussions

The model is numerically solved for velocity and temperature profiles using the Galerkin finite element method, and all computations are performed in Matlab. The range for the parameters  $H$ ,  $w_s$ ,  $F$ ,  $k_r$  and  $\varepsilon$  in this study are  $0 \leq H \leq 150$ ,  $-5 \leq w_s \leq 5$ ,  $0 \leq F \leq 10^5$ ,  $0.1 \leq k_r \leq 1$ ,  $0.1 \leq \varepsilon \leq 0.9$ .

### 4.1 Nusselt number profiles

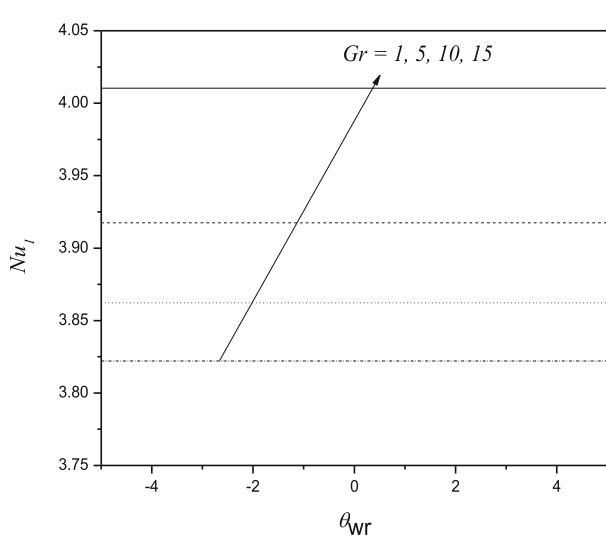
The influence of wall temperature ratio  $\theta_{wr}$  on Nusselt number  $Nu$  is observed in the following figures for the Regions-I, II and III. Region-I ( $-L \leq y \leq 0$ ) and Region-III ( $0 \leq y \leq L$ ) are occupied by the clear viscous fluid and Region-II ( $L \leq y \leq 2L$ ) is nano fluid saturated porous medium. The combined effect of Grashof number  $Gr$  and wall temperature ratio  $\theta_{wr}$  on Nusselt number is observed in Fig. 2 for all the three regions. As seen, in all three regions, increasing  $Gr$  causes an increase in the Nusselt number which is due to an increase in the wall temperature. However, heat transfer is found to be more in the nano fluid saturated porous channel when compared to the channels saturated with clear viscous fluids. Also, it is seen that Nusselt number is independent of  $\theta_{wr}$  in all the three regions for different values of  $Gr$ .

Figure 3 shows the effect of wall temperature ratio and Brinkman number on  $Nu$  using copper–water based nanofluid in the middle region. It is observed that an increase in the Brinkman number leads to decrease in the Nusselt number. This may be due to an increase in the temperature of the bulk fluid near the wall with the increase in the  $Br$ . However, heat transfer is found to be more in the nano fluid saturated porous channel when compared to the channels saturated with clear viscous fluids. For all different values of  $Br$ , it is found that there is no variation of  $Nu$  with the wall temperature ratio.

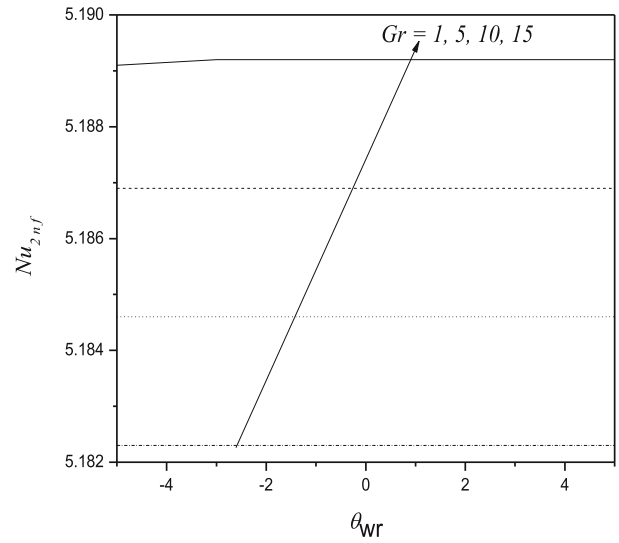
Figures 4 and 5 show the effect of solid volume fraction  $\phi$ , and porous parameter  $\sigma$  respectively on Nusselt number as the wall temperature ratio  $\theta_{wr}$  increases. A slight rise in the value of  $Nu$  is noticed with an increase in the values of  $\phi$  and  $\sigma$ . Increasing  $\sigma$  means decrease in the permeability of the porous medium. The velocity distribution appears to be more uniform with lower permeability, which contributes to an improvement in  $Nu$ . For various values of  $\phi$  and  $\sigma$ ,  $Nu$  values are found to be greater in the middle region compared to the other two end regions. The velocity reduces as the  $\phi$  increases. This finding can be explained by the fact that as nanoparticles are applied to a pure fluid, the concentration of the fluid increases and the fluid becomes denser, resulting in a reduction in the fluids velocity in the channel and an

**Table 1** Values of  $Nu$  for the values of  $P = 1, Br = 0.01, \phi = 0.02, \sigma = 4, H = F = k_r = w_s = w_f = 0$

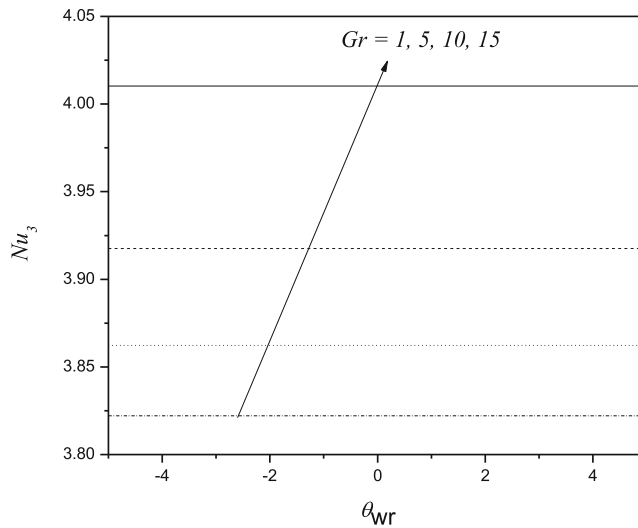
Gr	Present study		Umavathi and Hemvathi [18]		Ansys simulations	
	$(Nu_1)_{y=-1}$	$(Nu_3)_{y=2}$	$(Nu)_{y=-1}$	$(Nu)_{y=2}$	$(Nu)_{y=-1}$	$(Nu)_{y=2}$
1	0.3994	0.2738	0.3993	0.2737	0.3893	0.2747
5	0.4372	0.1972	0.4373	0.1973	0.4473	0.1973
10	0.5008	0.0588	0.5009	0.0589	0.5019	0.0599



(a) Region-I



(b) Region-II



(c) Region-III

**Fig. 2** Nusselt number profiles for different values of Grashof number  $Gr$

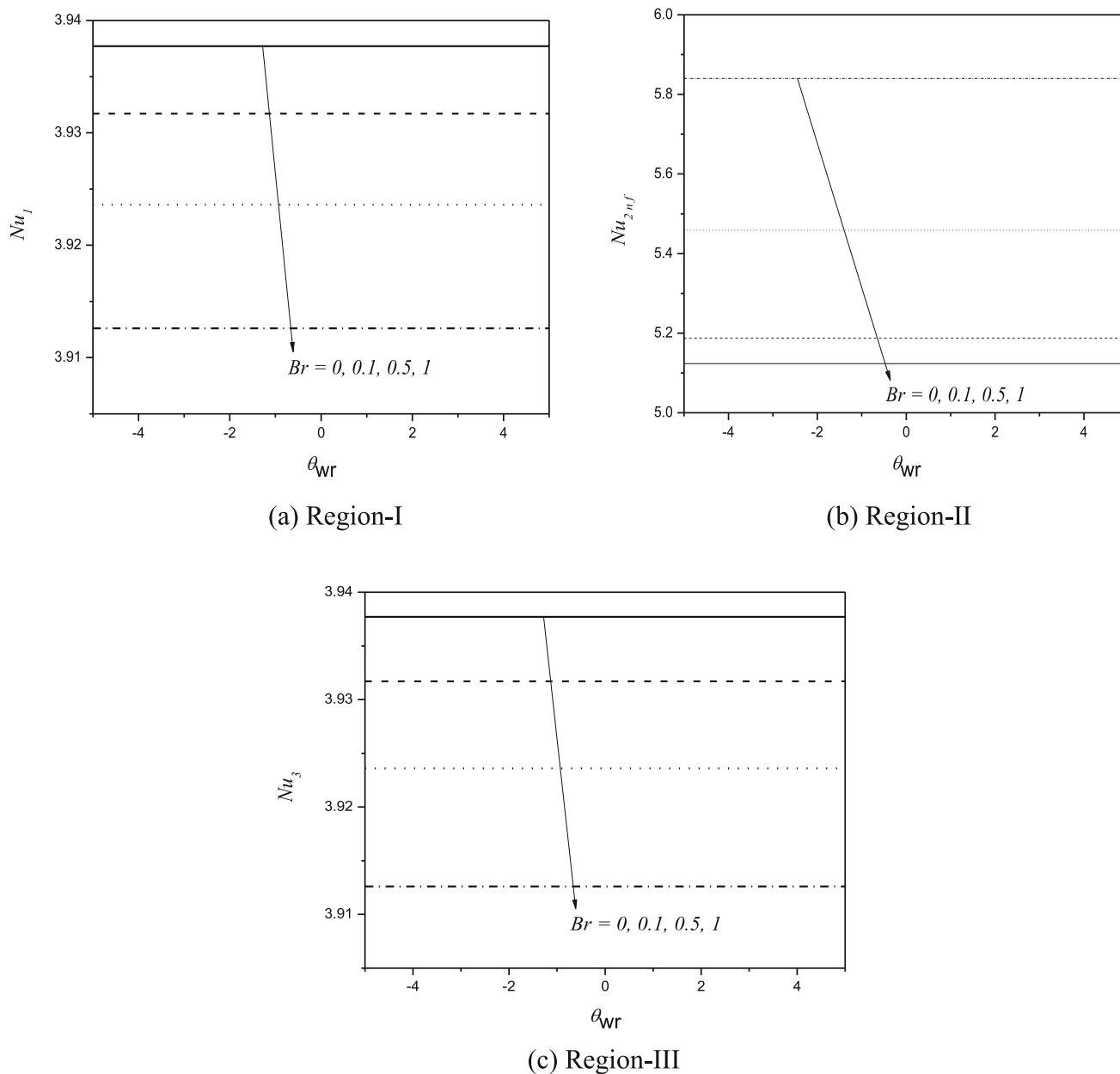


Fig. 3 Nusselt number profiles for differentt values of Brinkman number  $Br$

increase in  $Nu$ . For various values of  $\phi$  and  $\sigma$ , an increase in  $\theta_{wr}$  has no visible impact on  $Nu$  in any of the three regions.

Figure 6 depicts the effect of  $H$  on  $Nu$  as the increasing wall temperature ratio  $\theta_{wr}$ . It demonstrates that in a channel occupied with clear viscous fluid, the interphase heat transfer coefficient  $H$  does not influence  $Nu$ . In the middle region,  $Nu$  drops as  $H$  increases. Increasing the interface heat transfer coefficient, in other words, enhances thermal communications between the two phases of a porous material. As the temperature of the solid porous matrix falls, the temperature

of the nanofluid rises. As a consequence, the temperature difference between the nanofluid and the hot wall reduces, and the average Nusselt number of the nanofluid drops.

The effects of internal heat generation and wall temperature ratio on the  $Nu$  are displayed in Fig. 7 for all three regions, respectively. It has been noticed that increasing the internal-heat-generation values raises the Nusselt number in all three regions. When compared to the right and left walls of the channel, the effect of enhancement on the  $Nu$  is dominant in the middle region of the channel (saturated nanofluid-with porous media).

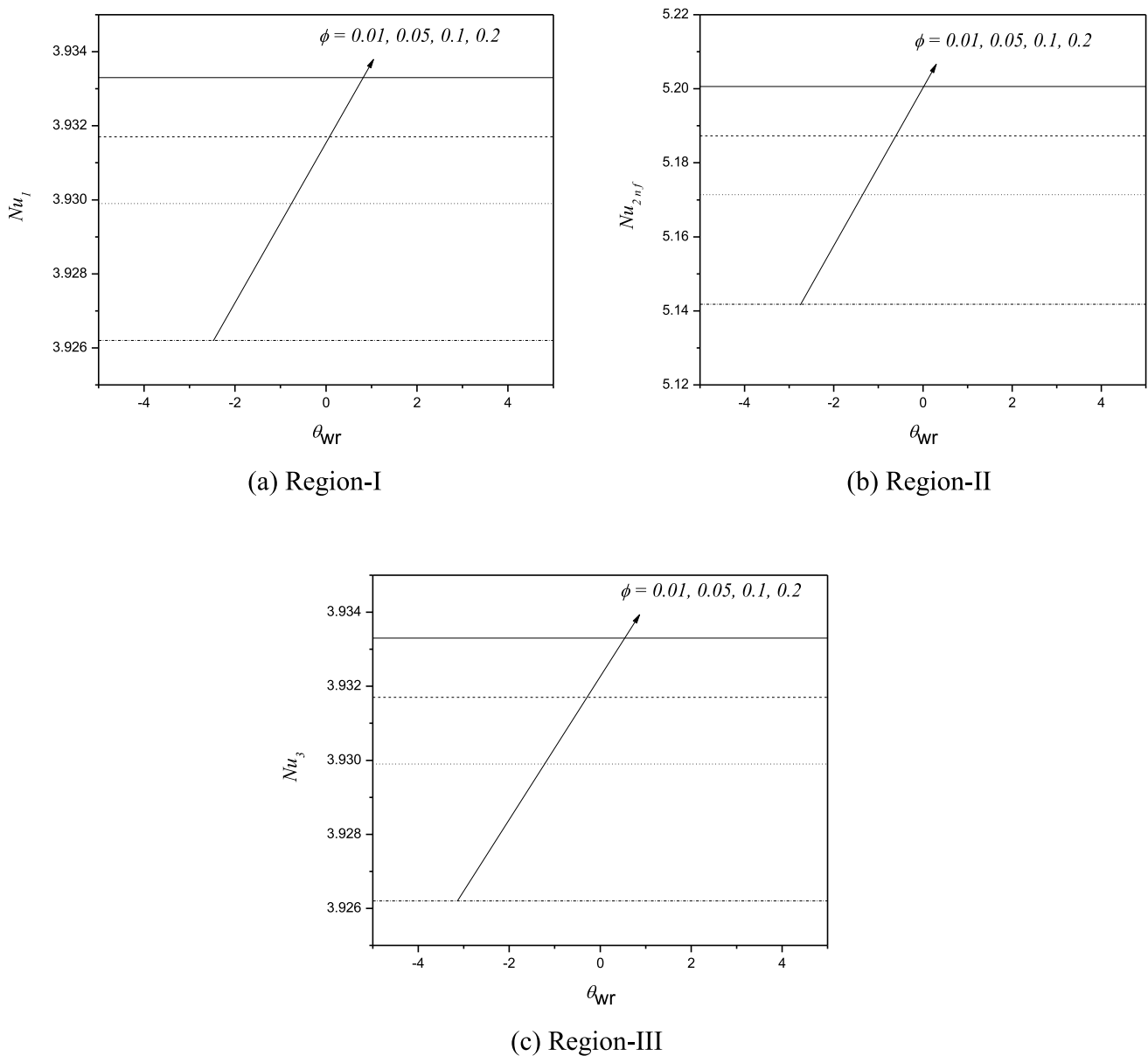


**Fig. 4** Nusselt number profiles for various values of solid volume fraction  $\phi$

The influence of the Forchheimer number  $F$  on the Nusselt number inside the enclosure is shown in Fig. 8a–c. It can be seen that when the  $F$  increases, the  $Nu$  decreases in all three regions. The influence of Forchheimer number is stronger in the middle region saturated with copper water-based nanofluid than on the right and left walls of the channels. A higher Forchheimer number indicates increased flow resistance, which leads to slower filtration and a lower Nusselt number.

The effect of the parameters nanofluid to solid porous matrix thermal conductivity ratio  $k_r$  and the porosity  $\varepsilon$  of the medium on Nusselt number are shown in Fig. 9a, b with the variable wall temperature ratio  $\theta_{wr}$ . Increase in  $k_r$  and

$\varepsilon$  leads to enhancement of Nusselt number. Hence it can be stated that porosity has a beneficial impact on the overall heat transfer rate. For various values of  $k_r$  and  $\varepsilon$ , it is discovered that the variable wall temperature ratio has no visible effect on the Nusselt number.

Figure 10a, b depict the influence of Grashof number  $Gr$  and Brinkman number  $Br$  respectively on Average Nusselt Number with the varying wall temperature ratio  $\theta_{wr}$ . Negative  $\theta_{wr}$  values indicate that one of the channel's walls is hot and the other is cold, whereas positive values imply that both walls are either hot or cold. As expected, increasing  $Gr$  induces an increase in wall temperature, which raises  $Nu$  and increasing  $Br$  causes the decrease in  $Nu$  which can be seen



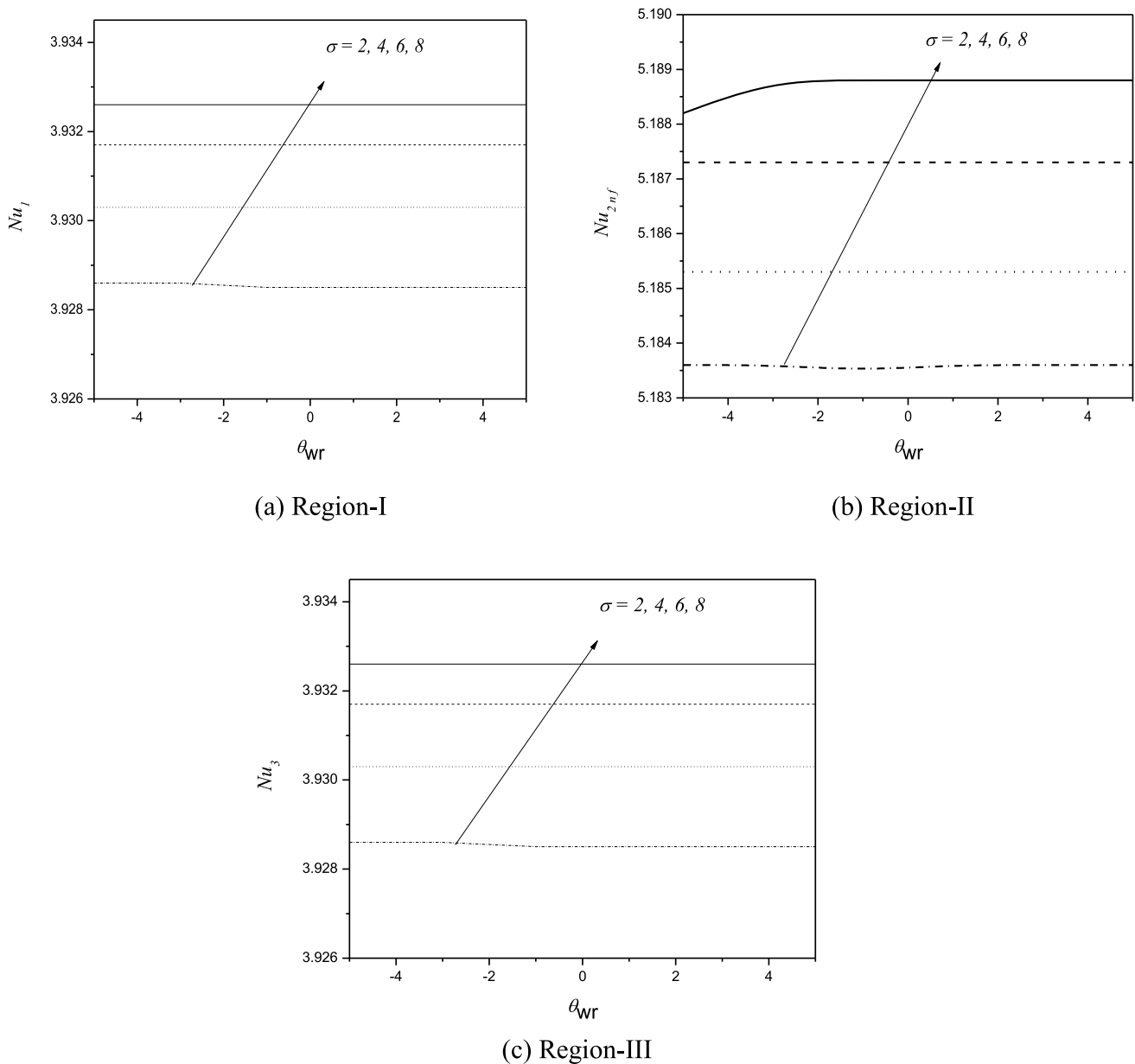


**Fig. 5** Nusselt number profiles for different values of porous parameter  $\sigma$

from the Fig. 10a, b respectively. These figures reveal that  $Nu$  decreases asymptotically to a common minimum value with varying  $\theta_{wr}$  from the negative values to positive values.

Figure 11a, b display the variation in  $Nu$  with the variation in the values of solid-volume-fraction  $\phi$  and the porous parameter  $\sigma$  respectively. According to these results,  $Nu$  appears to be less sensitive to changes in the values of  $\phi$  and  $\sigma$  which could be due to its effect on the small cross-sectional area of the porous region.  $Nu$ , on the other hand, increases in a negligible way as the values of  $\phi$  and  $\sigma$  increase.

The influence of the interphase heat transfer coefficient  $H$  and the Forchheimer number  $F$  on  $Nu$  is shown in Fig. 12a, b.

$Nu$  decreases when the heat transfer coefficient  $H$  rises, possibly due to rising fluid temperature profiles in the channel. It's also worth noting that  $Nu$  decreases as the Forchheimer number rises. With varying  $\theta_{wr}$  from negative to positive values, figures show that  $Nu$  decreases asymptotically to a common minimum value.

Figure 13a depicts the variations in  $Nu$  caused by simultaneous changes in the solid internal heat generation parameter and the wall temperature ratio. The heat absorption case of the solid corresponds to negative values of  $w_s$ , while the heat generation case corresponds to positive values of  $w_s$ . As  $w_s$  rises, the fluid warms, resulting in an increase in  $Nu$ . The

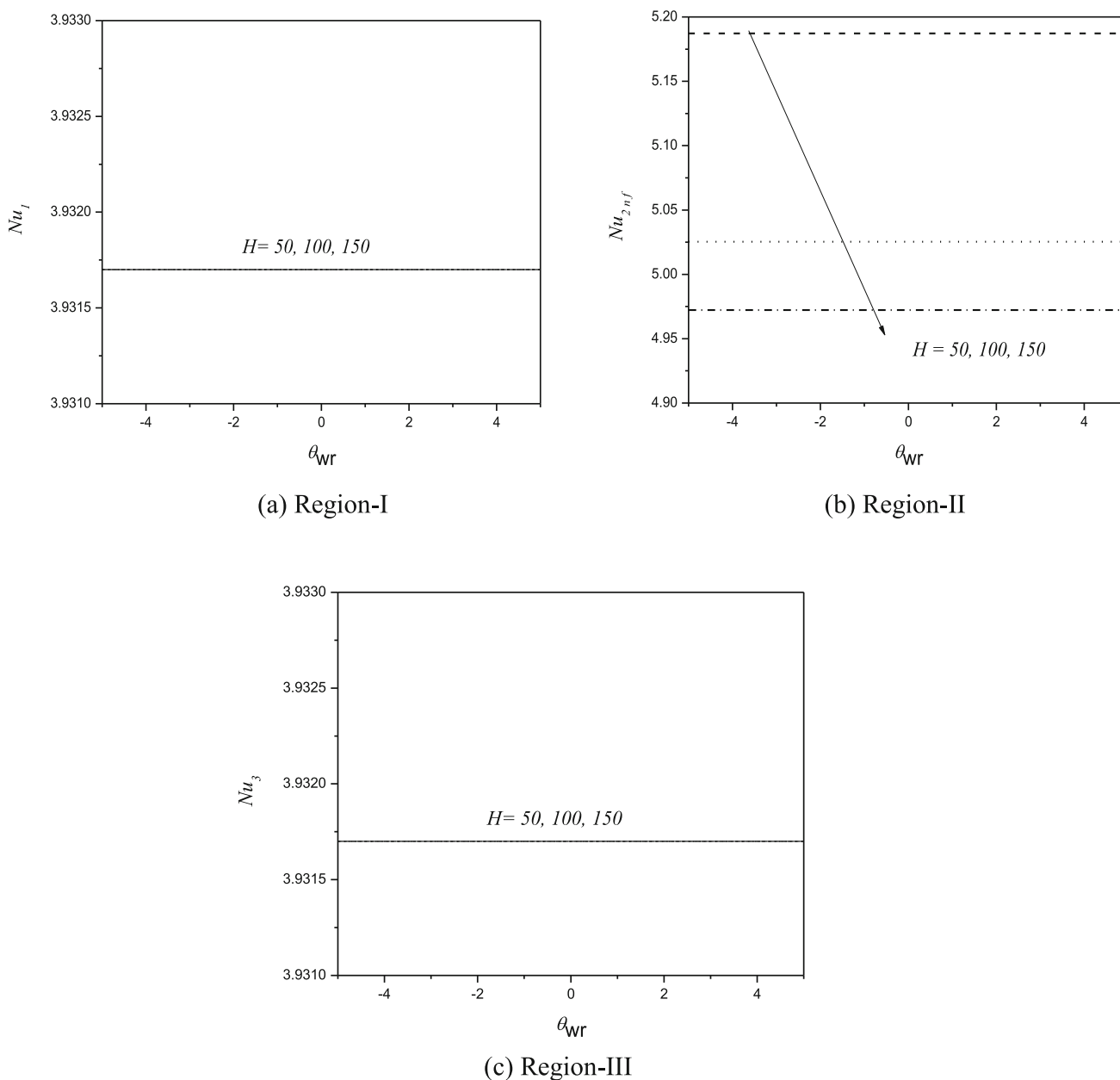


Fig. 6 Nusselt number profiles for various values of interphase heat transfer coefficient  $H$

effect of the nanofluid to solid porous matrix thermal conductivity ratio parameter  $k_r$  on  $Nu$  as the wall temperature ratio increases is shown in Fig. 13b. The consequence of the parameter  $k_r$  is that  $Nu$  increases as  $k_r$  rises, owing to an increase in the fluid’s thermal conductivity.

4.2 ANN model

Figure 14 depicts the ANN configuration model. The input parameters are  $Gr, Br, \phi, \sigma, H, F, w_s, k_r$  and  $\theta_{wr}$  and the output parameter is the Nusselt number. During the construction of an artificial neural network model, the available data

set is divided into two datasets. The first dataset 20% is used to train the ANN model, and the second dataset 80% is used to validate it. The predicted outcomes of the ANN model are compared to the remaining data. The proposed scheme employs four different types of back propagation algorithms: LMB, SCGB, BRB, and RB. Figure 14 shows how to reduce the error between expected output outcomes and input data by adjusting weights and biases. The numerical investigation’s dataset is used to create an optimal ANN model for forecasting heat transfer. The procedure for determining the best framework in the ANN is based on changing the number of neurons in a hidden layer and planning the ANN execution

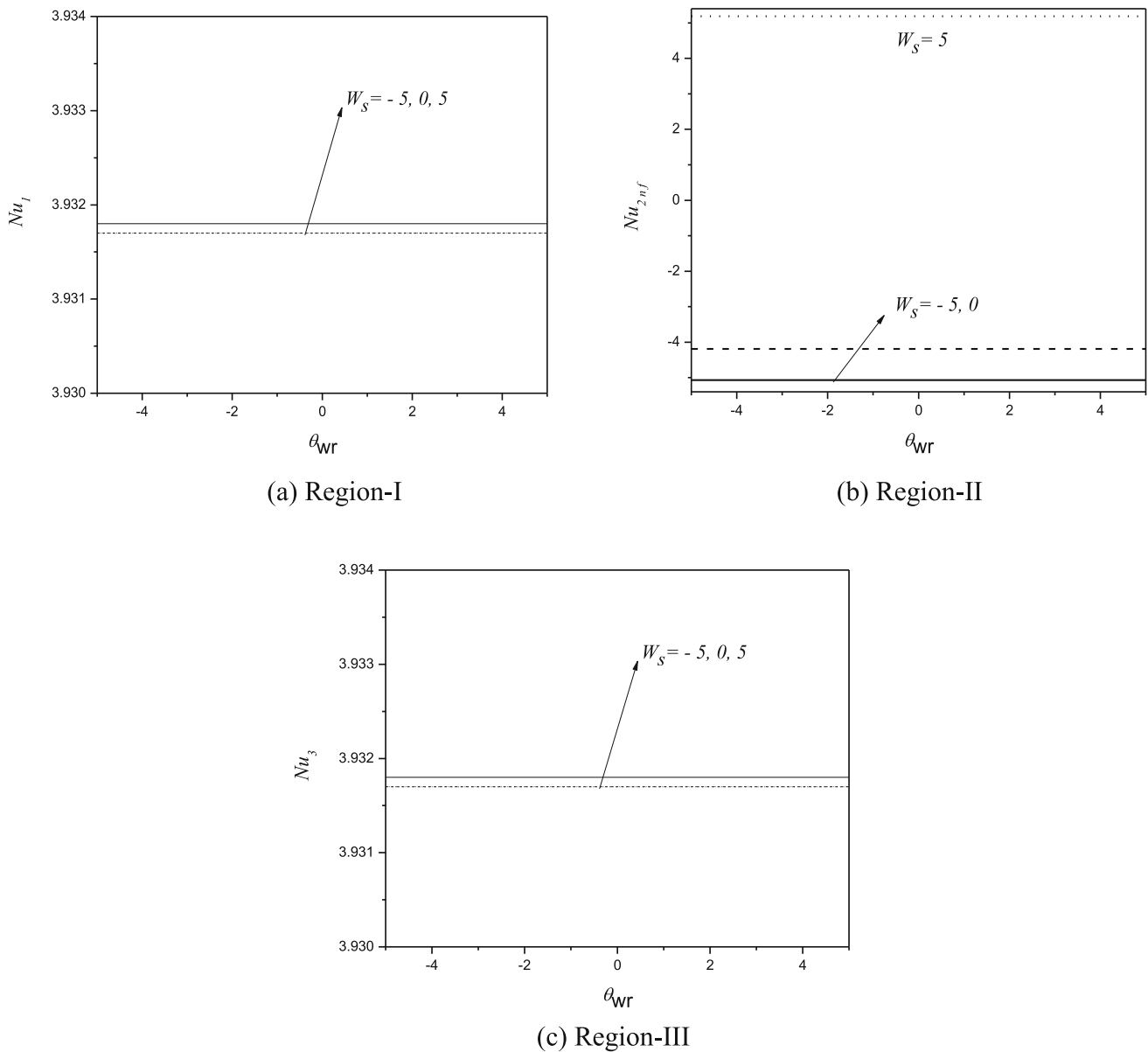


**Fig. 7** Nusselt number profiles for various solid internal-heat-generation  $w_s$  values

for each neuron number [42–46]. The optimal ANN’s results are more consistent with the theoretical dataset, and it can predict heat transfer better than the correlation, as shown in Fig. 14.

Table 2 demonstrates that the values for the  $Nu$  for all the governing parameters at three regions. The Nusselt number is maximum for silver nanoparticle in the left and middle regions and minimum for  $SiO_2$  and titanium oxide nanoparticle, whereas it is extreme for diamond nanoparticle and least for  $SiO_2$  nanoparticle in the right region respectively [47–50].

### 4.3 Velocity and temperature profiles

Table 3 demonstrates that the variations of velocity and temperature profiles for all the governing parameters at three regions. The amplitude of the increase in velocity is lower in region II when compared to region I and in region III when compared to region II because the fluid is saturated with porous media in the middle of the channel. The temperature profiles initially rise at the left wall (clear viscous fluid), then change to a parabolic shape in the middle of the

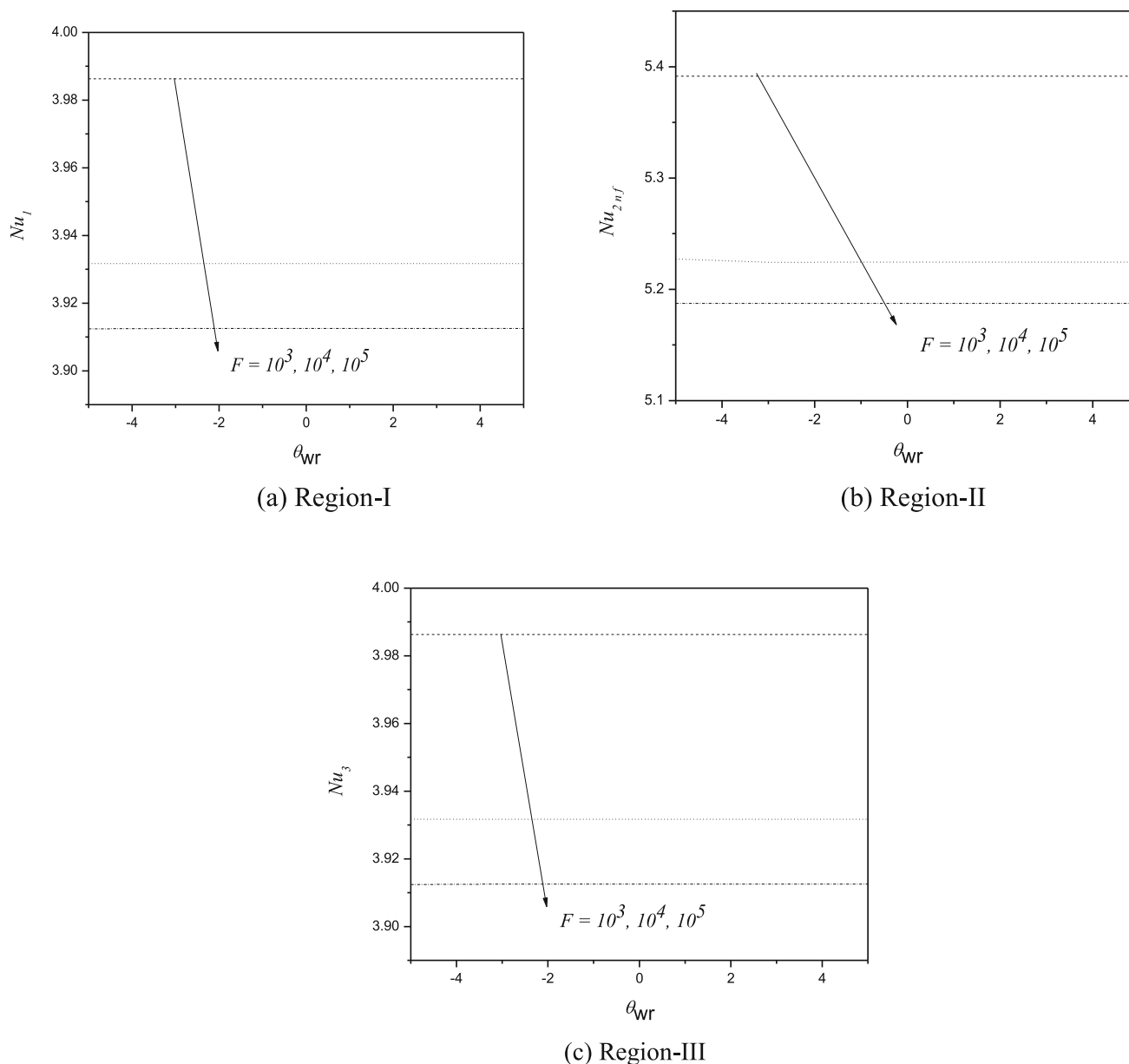


**Fig. 8** Profiles of Nusselt number for various values of Forchheimer numbers  $F$

channel (saturated nanofluid with porous media), then fall at the right wall (clear viscous fluid), and eventually reach one.

There are numerous methods and procedures used in the process of finding solutions to the numerous issues encountered in the manufacturing business [51–54]. Initially, the

experimental method was used to handle a broad variety of issues in the industrial sector [55–58]. Because of technological developments, testing methods can now be assessed and the outcomes of those tests can be predicted before the techniques are implemented [59–64].

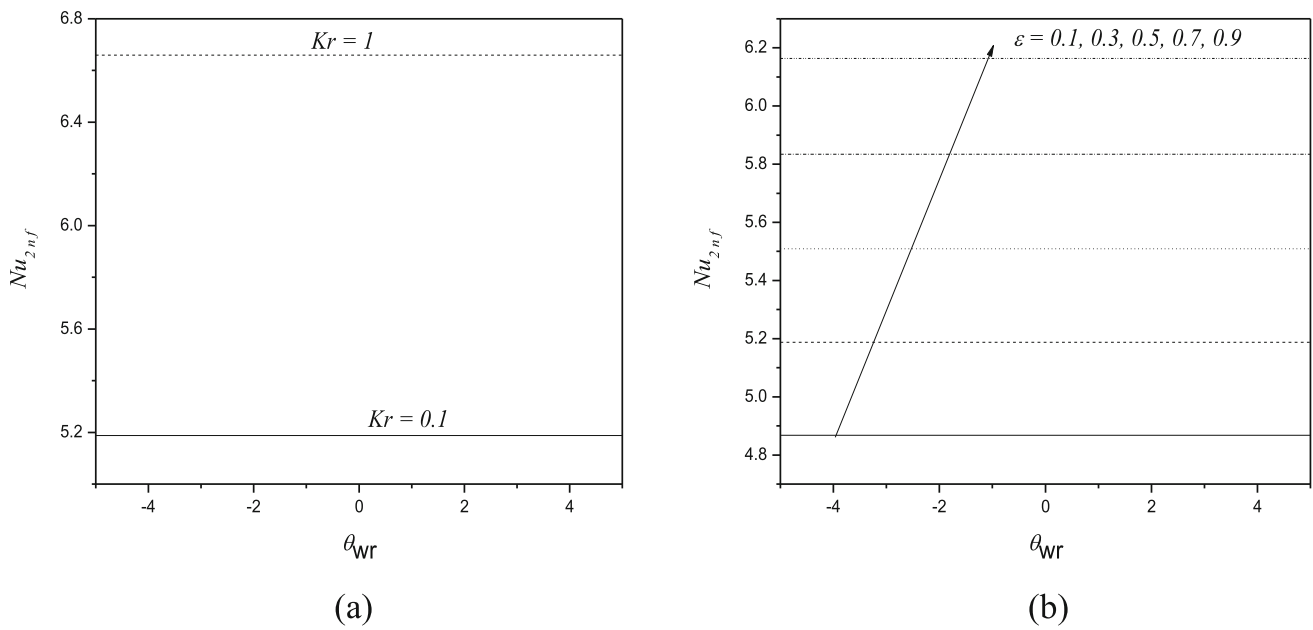


**Fig. 9** Profiles of Nusselt numbers for various values of **a** Nanofluid to solid porous matrix thermal conductivity ratio parameter  $k_r$ , **b** Porosity of the medium  $\varepsilon$ , Region-II

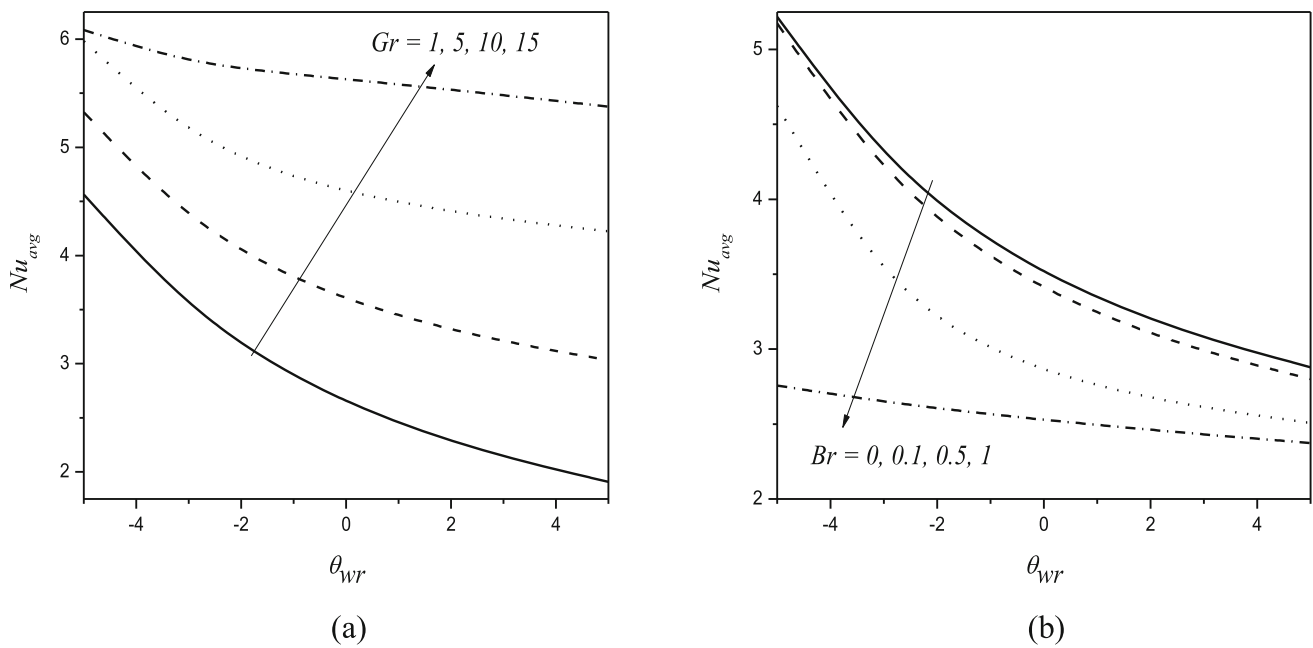


**Fig. 10** Profiles of average Nusselt numbers for various values of **a** Grashof number  $Gr$  **b** Brinkman number  $Br$

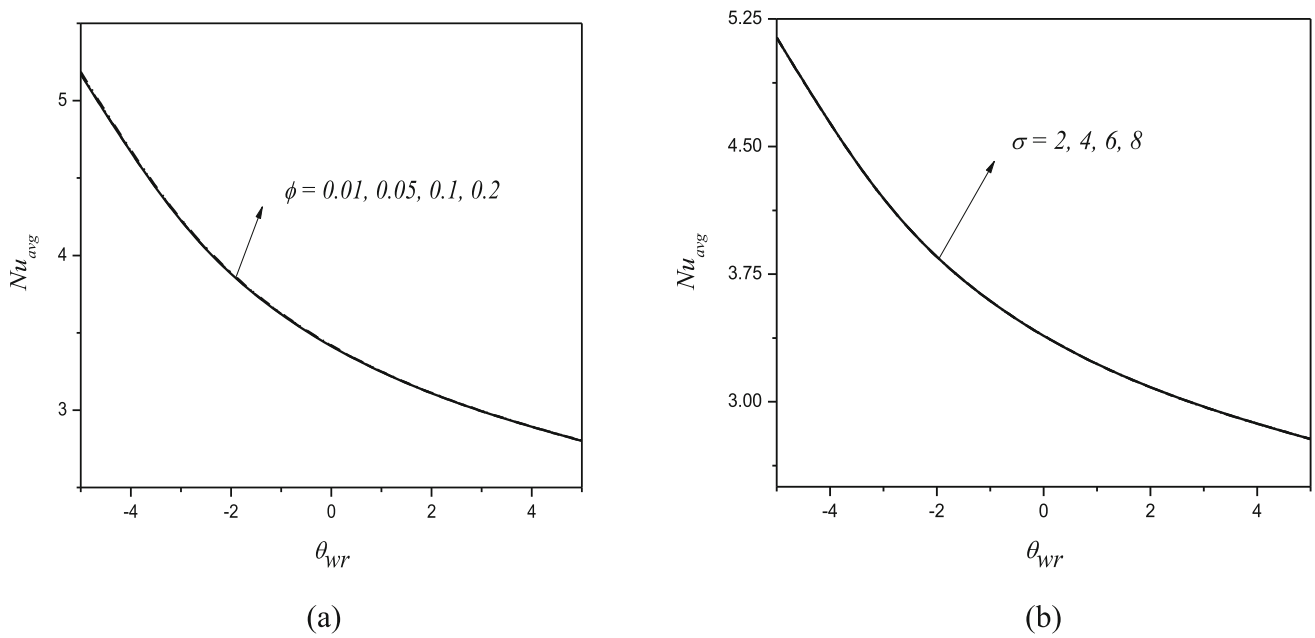


**Fig. 11** Average Nusselt number profiles for different values of **a** solid volume fraction  $\phi$ , **b** porous parameter  $\sigma$

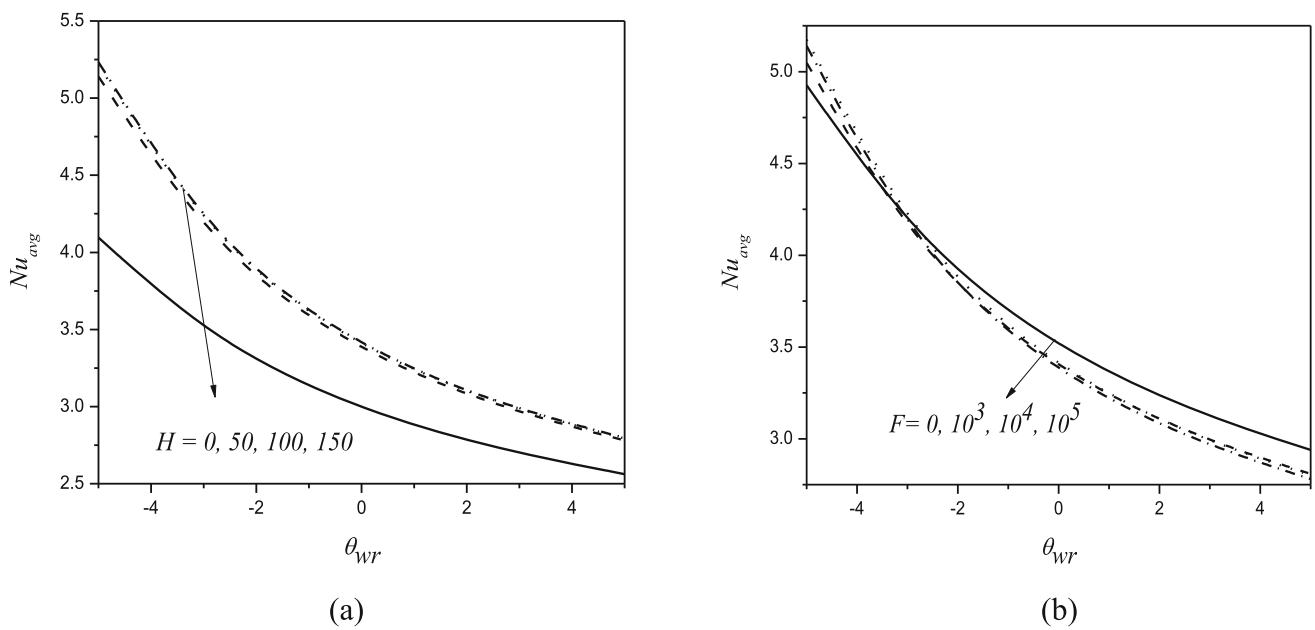


**Fig. 12** Average Nusselt number profiles for different values of **a** Interphase heat transfer coefficient  $H$ , **b** Forchheimer number  $F$

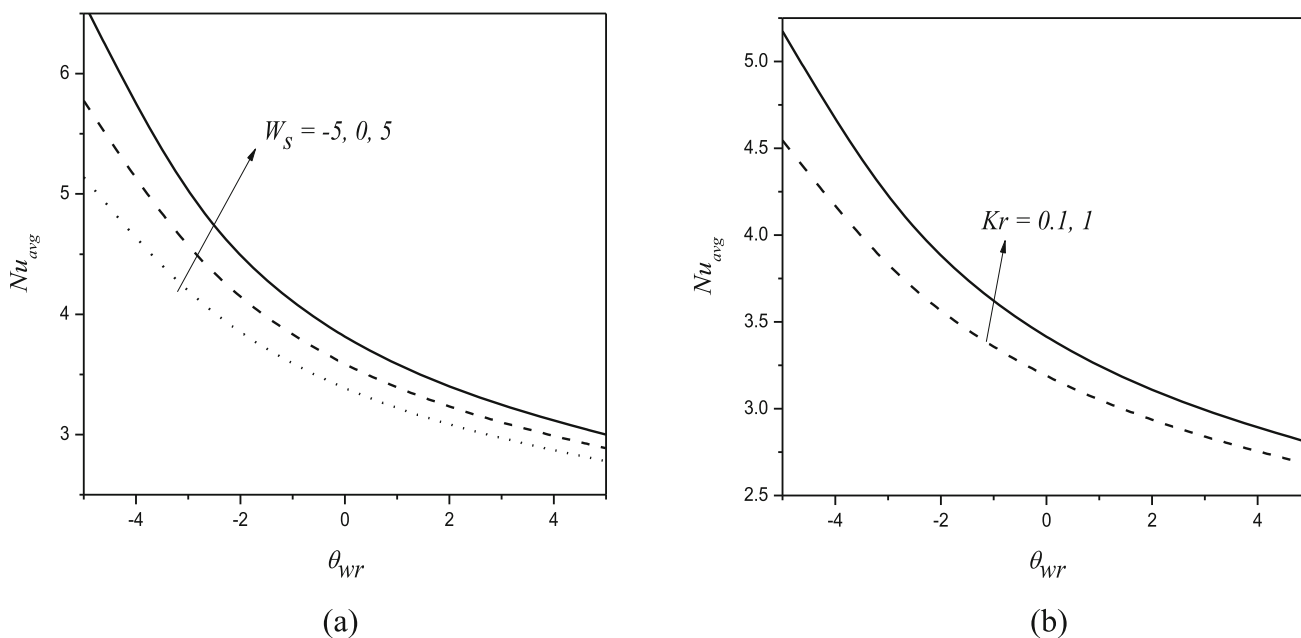


**Fig. 13** Average Nusselt number profiles for-various values of **a** solid internal heat-generation  $w_s$  **b** nanofluid to solid porous matrix thermal conductivity ratio parameter  $k_r$

**Table 3** Variations of velocity and temperature for the values of  $P = 5.0, Br = 0.1, \phi = 0.02, \sigma = 4, Gr = 5, H = F = 10, k_r = 1, w_s = 1, w_f = 0$

Region-I			Region-II				Region-III		
$y$	$u_1$	$\theta_1$	$y$	$u_2$	$\theta_{2nf}$	$\theta_{2ns}$	$y$	$u_3$	$\theta_3$
-1	0.000	0.000	0	0.9855	1.1165	0.9543	1	0.9866	1.2510
-0.5	1.8534	0.6552	0.5	0.5461	1.1972	1.1125	1.5	2.5612	1.1531
0	0.9845	1.1164	1	0.9856	1.2511	0.9446	2	0.000	1.1431

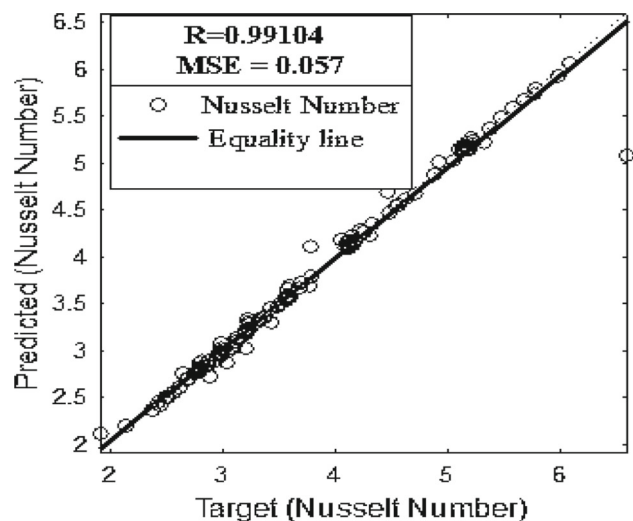


**Table 2** Values of Nusselt number fixing the values as  $Gr = 5, P = 1, Br = 0.01, \phi = 0.02, \sigma = 4, F = 10, H = 10, w_s = 5$  and  $\epsilon = 0.5$

Material	$Nu_1$	$Nu_{2f}$	$Nu_3$
Copper	3.62332	5.94235	3.62363
Silver	3.62436	5.94326	3.62195
SiO <sub>2</sub>	3.57525	5.92513	3.57506
Diamond	3.62351	5.92434	3.62544
TiO <sub>2</sub>	3.61243	5.42026	3.61258

**Fig. 14** Comparison between the theoretical data and the ANN outputs

## 5 Conclusions

Under local thermal nonequilibrium conditions, the effect of internal heat on heat transfer in a nanofluid saturated vertical channel with a porous matrix layer sandwiched between two fluid layers is investigated in this study. The Darcy—Forchheimer equation is used to simulate flow in a porous material. To characterize the nanofluid, the Tiwari and Das model is used. Using the Finite element Galerkin technique, the governing equations are transformed into matrix form. This equation system is solved for velocity and temperature profiles. The Nusselt number is calculated using these profiles. From this study, the following conclusions were drawn:

- Increasing the Grashof number and internal heat generation parameters improves heat transfer in all three regions.
- Heat transfer in the middle porous region, which is saturated with nanofluid, is observed to be higher than in regions one and three. Because the improvement in the thermal properties, including higher thermal conductivity and higher convective heat transfer coefficients than pure fluids.
- The heat transfer in all three regions was reduced as the Forchheimer number and Brinkman number were increased.
- Heat transfer in the middle region is reduced when inter-phase heat transfer is increased.
- Heat transfer was optimal when silver was employed as a nanoparticle. However, heat transfer was poor when titanium oxide was used.

## Declarations

**Conflict of interest** None declared.

## References

1. Bello, O., Reinicke, K.M., Teodoriu, C.: Particle holdup profiles in horizontal gas-liquid- solid multiphase flow pipeline. *Chem. Eng. Technol.* **28**(12), 1546–1553 (2005)
2. Miao, Q., Zhu, J., Barghi, S., Chuangzhi, W., Yin, X., Zhou, Z.: Modeling biomass gasification in circulating fluidized beds. *Renew. Energy* **50**, 65–661 (2013)
3. Scott, D.S., Rao, P.K.: Transport of solids by gas-liquid mixtures in horizontal pipes. *Can. J. Chem. Eng.* **49**(3), 302–309 (1971)
4. Mao, F., Desir, F.K., Ebadian, M.A.: Pressure drop measurement and correlation for three-phase flow of simulated nuclear waste in a horizontal pipe. *Int. J. Multiph. Flow* **23**(2), 397–402 (1997)
5. Orell, A.: The effect of gas injection on the hydraulic transport of slurries in horizontal pipes. *Chem. Eng. Sci.* **62**(23), 6659–6676 (2007)
6. Ghasemi, M.H., Hoseinzadeh, S., Heyns, P.S., Wilke, D.N.: Numerical analysis of non-Fourier heat transfer in a solid cylinder with dual-phase-lag phenomenon. *Comput. Model. Eng. Sci.* **122**(1), 399–414 (2020)
7. Vafai, K., Kim, S.J.: Fluid mechanics of the interface region between a porous medium and a fluid layer—an exact solution. *Int. J. Heat Fluid Flow* **11**(3), 254–256 (1990)
8. Alazmi, B., Vafai, K.: Analysis of fluid flow and heat transfer interfacial conditions between a porous medium and a fluid Layer. *Int. J. Heat Mass Transf.* **44**, 1735–1749 (2001)
9. Kuznetsov, A.V., Vafai, K.: Development and investigation of three-phase model of the mushy zone for analysis of porosity formation in solidifying castings. *Int. J. Heat Mass Transf.* **38**(14), 2557–2567 (1995)
10. Chen, Z., Ewing, R.E.: Comparison of various formulations of three-phase flow in porous media. *J. Comput. Phys.* **132**, 362–373 (1997)
11. Malashetty, M.S., Umavathi, J.C., Prathap Kumar, J.: Two fluid flow and heat transfer in an inclined channel containing porous and fluid layer. *Heat Mass Transf.* **40**, 871–876 (2004)
12. Malashetty, M.S., Umavathi, J.C., Prathap Kumar, J.: Flow and heat transfer in an inclined channel containing fluid layer sandwiched between two porous layers. *J. Porous Media* **8**(5), 443–453 (2005)
13. Cheng, L., Ghajar, A.J.: Frontiers and progress in multiphase flow and heat transfer. *Heat Transf. Eng.* **40**(16), 1299–1300 (2018)
14. Dong, J., Inthavong, K., Tu, J. (2016). *Multiphase Flows in Biomedical Applications*. In: Yeoh, G. (eds) *Handbook of Multiphase Flow Science and Technology*. Springer, Singapore. [https://doi.org/10.1007/978-981-4585-86-6\\_16-1](https://doi.org/10.1007/978-981-4585-86-6_16-1)
15. Umavathi, J.C., Malashetty, M.S., Mateen, A.: Fully developed flow and heat transfer in a horizontal channel containing electrically conducting fluid sandwiched between two fluid layers. *Int. J. Appl. Mech. Eng.* **9**(4), 781–794 (2004)
16. Umavathi, J.C., Chamkha, A.J., Manjula, M.H., Al Mudhaf, A.: Flow and heat transfer of a couple-stress fluid sandwiched between viscous fluid layers. *Can. J. Phys.* **83**, 05–035 (2005)
17. Umavathi, J.C., Liu, I.C., Prathap Kumar, J., Shaik Meera, D.: Unsteady flow and heat transfer of porous media sandwiched between viscous fluids. *Appl. Math. Mech.* **31**, 1497–1516 (2010)
18. Umavathi, J.C., Hemavathi, K.: Flow and heat transfer of composite porous medium saturated with nanofluid. *Propuls. Power Res.* **8**(2), 173–181 (2019)
19. Patra, A.K., Nayak, M.K., Misra, A.: Viscosity of nanofluids—a Review. *Int. J. Thermofluid Sci. Technol.* **7**(2), 070202 (2020)
20. Molli, S., Naikoti, K.: MHD natural convective flow of Cu-water nanofluid over a past infinite vertical plate with the presence of time dependent boundary condition. *Int. J. Thermofluid Sci. Technol.* **7**(4), 070404 (2020)
21. Hoseinzadeh, S., Taheri Otagh Sara, S.M., Zakeri Khatir, M.H., Heyns, P.S.: Numerical investigation of thermal pulsating alumina/water nanofluid flow over three different cross-sectional channel. *Int. J. Numer. Methods Heat Fluid Flow* **30**(7), 3721–3735 (2020)
22. Nakayama, A., Kokudai, T., Koyama, H.: Non-Darcian boundary layer flow and forced convective heat transfer over a flat plate in a fluid-saturated porous medium. *ASME J. Heat Transf.* **112**, 157–162 (1990)
23. Bear, J.: *Dynamics of Fluids in Porous Media*. Elsevier, New York (1972)
24. Nield, D.A., Bejan, A.: *Convection in Porous Media*, 4th edn. Springer, New York (2013)
25. Mahmoudi, Y.: Constant wall heat flux boundary condition in micro-channels filled with a porous medium with internal heat generation under local thermal non-equilibrium condition. *Int. J. Heat Mass Transf.* **85**, 524–542 (2015)



26. Dehghan, M., Valipour, M.S., Saedodin, S., Mahmoudi, Y.: Investigation of forced convection through entrance region of a porous-filled microchannel: an analytical study based on the scale analysis. *Appl. Therm. Eng.* **99**, 446–454 (2016)
27. Yang, K., Vafai, K.: Analysis of temperature gradient bifurcation in porous media—an exact solution. *Int. J. Heat Mass Transf.* **53**, 4316–4325 (2010)
28. Dehghan, M., Valipour, M.S., Saedodin, S.: Microchannels enhanced by porous materials: heat transfer enhancement or pressure drop increment. *Energy Convers. Manag.* **110**, 22–32 (2016)
29. Dickson, C., Torabi, M., Karimi, N.: First and second law analyses of nanofluid forced convection in a partially-filled porous channel—the effects of local thermal non-equilibrium and internal heat sources. *Appl. Therm. Eng.* **103**, 459–480 (2016)
30. Hoseinzadeh, S., Heyns, P.S., Chamkha, A.J., Shirkhani, A.: Thermal analysis of porous fins enclosure with the comparison of analytical and numerical methods. *J. Therm. Anal. Calorim.* **138**, 727–735 (2019)
31. Ghanbari Ashrafi, T., Hoseinzadeh, S., Sohani, A., Shahverdian, M.H.: Applying homotopy perturbation method to provide an analytical solution for Newtonian fluid flow on a porous flat plate. *Math Meth. Appl. Sci.* **44**, 7017–7030 (2021)
32. Hoseinzadeh, S., Sohani, A., Ghanbari Ashraf, T.: An artificial intelligence-based prediction way to describe flowing a Newtonian liquid/gas on a permeable fat surface. *J. Therm. Anal. Calorim.* (2021). <https://doi.org/10.1007/s10973-019-08203-x>
33. Tiwari, R.K., Das, M.K.: Heat transfer augmentation in a two-sided lid-driven differentially heated square cavity utilizing nanofluids. *Int. J. Heat Mass Transf.* **50**, 2002–2018 (2007)
34. Ghasemi, B., Aminossadati, S.M.: Natural convection heat transfer in an inclined enclosure filled with a water-CuO nanofluid. *Numer. Heat Transf.* **55**, 807–823 (2009)
35. Muthumalyselvan, M., Kandaswamy, P., Lee, J.: Heat transfer enhancement of copper-water nanofluids in a lid-driven enclosure. *Commun. Nonlinear Sci. Numer. Simul.* **15**, 1501–1510 (2010)
36. Vajravelu, K., Prasad, K.V., Abbasandy, S.: Convective transport of nanoparticles in multi-layer fluid flow. *Appl. Math. Mech.-Eng. Ed.* **34**, 177–188 (2013)
37. Seetharamu, K.N., Leela, V., Kotlani, N.: Numerical investigation of heat transfer in a micro-porous-channel under variable wall heat flux and variable wall temperature boundary conditions using local thermal non-equilibrium model with internal heat generation. *Int. J. Heat Mass Transf.* **112**, 201–215 (2017)
38. Brinkman, H.C.: Viscosity of concentrated suspensions and solutions. *J. Chem. Phys.* **20**, 571–581 (1952)
39. Maxwell, J.: *A Treatise on Electricity and Magnetism*, 2nd edn. Oxford University Press, Cambridge (1904)
40. Lewis, R.W., Nithiarasu, P., Seetharamu, K.N.: *Fundamentals of Finite Element Method for Heat and Fluid Flow*. Wiley, Hoboken (2004)
41. Nithiarasu, P., Lewis, R.W., Seetharamu, K.N.: *Fundamentals of Finite Element Method for Heat and Mass Transfer*, 2nd edn. Wiley, Hoboken (2016)
42. Agarwal, K.M., Tyagi, R.K., Saxena, K.K.: Deformation analysis of Al alloy AA2024 through equal channel angular pressing for aircraft structures. *Adv. Mater. Process. Technol.* **8**(1), 828–842 (2022)
43. Bandhu, D., Kumari, S., Prajapati, V., Saxena, K.K., Abhishek, K.: Experimental investigation and optimization of RMDTM welding parameters for ASTM A387 grade 11 steel. *Mater. Manuf. Process.* **36**(13), 1524–1534 (2021)
44. Durga Prasad, C., Joladarashi, S., Ramesh, M.R., Srinath, M.S.: Microstructure and tribological resistance of flame sprayed CoMoCrSi/WC-CrC-Ni and CoMoCrSi/WC-12Co composite coatings remelted by microwave hybrid heating. *J. Bio Tribo-Corros.* **6**, 124 (2020). <https://doi.org/10.1007/s40735-020-00421-3>
45. Durga Prasad, C., Joladarashi, S., Ramesh, M.R.: Comparative investigation of HVOF and flame sprayed CoMoCrSi coating. *Am. Inst. Phys.* **2247**, 050004 (2020). <https://doi.org/10.1063/5.0003883>
46. Durga Prasad, C., Jerri, A., Ramesh, M.R.: Characterization and sliding wear behavior of iron based metallic coating deposited by HVOF process on low carbon steel substrate. *J. Bio Tribo-Corros.* **6**, 69 (2020). <https://doi.org/10.1007/s40735-020-00366-7>
47. Beniwal, G., Saxena, K.K.: A review on pore and porosity in tissue engineering. *Mater. Today Proc.* **44**, 2623–2628 (2021)
48. Dhawan, A., Gupta, N., Goyal, R., Saxena, K.K.: Evaluation of mechanical properties of concrete manufactured with fly ash, bagasse ash and banana fibre. *Mater. Today Proc.* **44**, 17–22 (2021)
49. Durga Prasad, C., Joladarashi, S., Ramesh, M.R., Srinath, M.S., Channabasappa, B.H.: Effect of microwave heating on microstructure and elevated temperature adhesive wear behavior of HVOF deposited CoMoCrSi-Cr<sub>3</sub>C<sub>2</sub> composite coating. *Surf. Coat. Technol.* **374**, 291–304 (2019). <https://doi.org/10.1016/j.surfcoat.2019.05.056>
50. Durga Prasad, C., Joladarashi, S., Ramesh, M.R., Srinath, M.S., Channabasappa, B.H.: Development and sliding wear behavior of Co-Mo-Cr-Si cladding through microwave heating. *SILICON* **11**, 2975–2986 (2019). <https://doi.org/10.1007/s12633-019-0084-5>
51. Durga Prasad, C., Joladarashi, S., Ramesh, M.R., Srinath, M.S., Channabasappa, B.H.: Microstructure and tribological behavior of flame sprayed and microwave fused CoMoCrSi/CoMoCrSi-Cr<sub>3</sub>C<sub>2</sub> coatings. *Mater. Res. Express* **6**, 026512 (2019). <https://doi.org/10.1088/2053-1591/aeabd9>
52. Durga Prasad, C., Joladarashi, S., Ramesh, M.R., Srinath, M.S., Channabasappa, B.H.: Influence of microwave hybrid heating on the sliding wear behaviour of HVOF sprayed CoMoCrSi coating. *Mater. Res. Express* **5**, 086519 (2018). <https://doi.org/10.1088/2053-1591/aad44e>
53. Durga Prasad, C., Joladarashi, S., Ramesh, M.R., Sarkar, A.: High temperature gradient cobalt based clad developed using microwave hybrid heating. *Am. Inst. Phys.* **1943**, 020111 (2018). <https://doi.org/10.1063/1.5029687>
54. Gupta, N., Gupta, A., Saxena, K.K., Shukla, A., Goyal, S.K.: Mechanical and durability properties of geopolymer concrete composite at varying superplasticizer dosage. *Mater. Today Proc.* **44**, 12–16 (2021)
55. Kodli, B.K., Karre, R., Saxena, K.K., Pancholi, V., Dey, S.R., Bhattacharjee, A.: Flow behaviour of TiHy 600 alloy under hot deformation using gleeble 3800. *Adv. Mater. Process. Technol.* **3**(4), 490–510 (2017)
56. Kumar, K.B., Saxena, K.K., Dey, S.R., Pancholi, V., Bhattacharjee, A.: Peak stress studies of hot compressed TiHy 600 alloy. *Mater. Today Proc.* **4**(8), 7365–7374 (2017)
57. Kumar, N., Bharti, A., Saxena, K.K.: A re-investigation: effect of powder metallurgy parameters on the physical and mechanical properties of aluminium matrix composites. *Mater. Today Proc.* **44**, 2188–2193 (2021)
58. Durga Prasad, C., Lingappa, S., Joladarashi, S., Ramesh, M.R., Sachin, B.: Characterization and sliding wear behavior of CoMoCrSi+Flyash composite cladding processed by microwave irradiation. *Mater. Today Proc.* **46**, 2387–2391 (2021). <https://doi.org/10.1016/j.matpr.2021.01.156>
59. Reddy, M.S., Durga Prasad, C., Patil, P., Ramesh, M.R., Rao, N.: Hot corrosion behavior of plasma sprayed NiCrAlY/TiO<sub>2</sub> and NiCrAlY/Cr<sub>2</sub>O<sub>3</sub>/YSZ cermet coatings on alloy steel. *Surf. Interfaces* **22**, 100810 (2021). <https://doi.org/10.1016/j.surf.2020.100810>
60. Durga Prasad, C., Joladarashi, S., Ramesh, M.R., Srinath, M.S., Channabasappa, B.H.: Comparison of high temperature wear

- behavior of microwave assisted HVOF sprayed CoMoCrSi-WC-CrC-Ni/WC-12Co composite coatings. *SILICON* **12**, 3027–3045 (2020). <https://doi.org/10.1007/s12633-020-00398-1>
61. Vasudev, H., Prashar, G., Thakur, L., Bansal, A.: Electrochemical corrosion behavior and microstructural characterization of HVOF sprayed inconel718-Al<sub>2</sub>O<sub>3</sub> composite coatings. *Surf. Rev. Lett.* **29**, 2250017 (2022). <https://doi.org/10.1142/S0218625X22500172>
  62. Vasudev, H., Prakash, C.: Surface engineering and performance of biomaterials: editorial. *J. Electrochem. Sci. Eng.* **13**(1), 1–3 (2023). <https://doi.org/10.5599/jese.1698>
  63. Singh, M., Vasudev, H., Singh, M.: Surface protection of SS-316L with boron nitride based thin films using radio frequency magnetron sputtering technique: original scientific paper. *J. Electrochem. Sci. Eng.* **12**(5), 851–863 (2022). <https://doi.org/10.5599/jese.1247>
  64. Sandhu, K., Singh, G., Singh, S., Kumar, R., Prakash, C., Ramakrishna, S., Królczyk, G., Pruncu, C.I.: Surface characteristics of machined polystyrene with 3D printed thermoplastic tool. *Materials*. **13**, 2729 (2020)

**Publisher's Note** Springer Nature remains neutral with regard to jurisdictional claims in published maps and institutional affiliations.

Springer Nature or its licensor (e.g. a society or other partner) holds exclusive rights to this article under a publishing agreement with the author(s) or other rightsholder(s); author self-archiving of the accepted manuscript version of this article is solely governed by the terms of such publishing agreement and applicable law.